



Design and scale-up of a Cr-free Fe-Al-Cu catalyst for hydrogen production from waste-derived synthesis gas

Won-Jun Jang^a, Jae-Oh Shim^a, Kyung-Won Jeon^a, Hyun-Suk Na^a, Hak-Min Kim^a, Yeol-Lim Lee^a, Hyun-Seog Roh^{a,*}, Dae-Woon Jeong^{b,*}

^a Department of Environmental Engineering, Yonsei University, 1 Yonseidaegil, Wonju, Gangwon 26493, Republic of Korea

^b School of Civil, Environmental and Chemical Engineering, Changwon National University, 20 Changwondaehak-ro, Changwon, Gyeongnam 51140, Republic of Korea

ARTICLE INFO

Keywords:

Cr-free
Water gas shift
Hydrogen production
Waste-derived synthesis gas
Scale-up

ABSTRACT

Herein, we have prepared a series of Cr-free Fe-Al-Cu catalysts by the homogeneous one-step co-precipitation method and examined their ability to promote the water gas shift (WGS) reaction and thus facilitate the production of hydrogen from waste-derived synthesis gas. The prepared catalysts are confirmed to possess γ -Fe₂O₃, which can be more easily transformed into Fe₃O₄ than α -Fe₂O₃. The surface area, Fe₃O₄ crystallite size, reducibility, and Cu dispersion of these catalysts significantly depend on the concentrations of metal precursor. The catalysts effectively promote the WGS reaction without facilitating undesirable side reactions, achieving efficient hydrogen production and high CO conversion. The characteristics of the best-performing sample are preserved when the production is scaled up by a factor of 40 and thus obtained large-scale Fe-Al-Cu catalyst exhibits excellent reducibility and high CO conversion. Both commercial Fe-Cr and large-scale Fe-Al-Cu catalysts achieve close-to-equilibrium CO conversions at a gas hourly space velocity (GHSV) of 3000 mL g⁻¹ h⁻¹, but the latter showed a higher conversion than the former at a GHSV of 40,057 mL g⁻¹ h⁻¹ owing to the promotional effect of Cu on the easier reducibility of Fe species and the formation of additional Cu active sites. Thus, we demonstrate the possibility of finding Cr-free alternatives and show that the reducibility, Fe₃O₄ crystallite size, and Cu dispersion of the best-performing catalyst could be maintained upon upscaling, which made this catalyst well suited for converting waste-derived synthesis gas into H₂.

1. Introduction

Progress in catalysis has been always motivated by societal needs such as environment, energy, chemicals, or fuels [1,2]. As industry faces the pressure for the development of environmental-friendly processes, converging technologies are the new paradigm of research. This provides a tremendous opportunity in improving traditional technologies, but it also demands the catalyst for the new technology [3]. Likewise, waste management is one of a traditional technology and a primary challenge in developing countries, as exemplified by the cases of Korea, India, and China, which are the fastest growing economies in view of the development of energy-intensive industries over the past several decades [4]. Diverse system and policy such as extended producer responsibility, volume-based waste fee and 3R (Reduce, reuse and recycle) have been implemented to mitigate the problems of waste generation and resource consumption accompanying economy growth [5,6]. However, the total amount of generated waste is still on the rise, in line with the increase of GDP, and a considerable fraction of this waste still ends up in landfills [7]. To mitigate this problem and facilitate the recovery of energy from

waste, the 4R (reduce, reuse, recycle, and recover) policy has been introduced, focusing on the shift of material recycling to energy recovery in line with the so-called “waste-to-energy” (WtE) strategy [8]. The gasification of waste allows waste to be converted into gaseous products (CO, H₂, CH₄, and CO₂), and its hazardous components are destroyed at the high operating temperature of gasification [9,10]. However, a wide range of product composition restrict their use in advanced applications for producing fuels and chemicals. In our previous corroborative study, therefore, our groups have been firstly directed at establishing a sustainable and cost-effective method of hydrogen production waste gasification combined with the high-temperature water gas shift (HT-WGS, CO + H₂O ↔ H₂ + CO₂, ΔH = -41.2 kJ/mol) reaction [11–14]. However, there were significant challenges posed by the use of conventional HT-WGS catalysts [11,12]. One of such challenges is the requirement of high hydrogen production efficiency per unit hour in view of the higher CO content of waste-derived synthesis gas (~40 vol%) compared to that of natural gas-derived conventional synthesis gas (~10 vol%). Another challenge is the need to substitute the harmful Cr in the commercial catalyst (Fe₃O₄-Cr₂O₃) for more environmentally benign

* Corresponding authors.

E-mail addresses: hsroh@yonsei.ac.kr (H.-S. Roh), dwjeong@changwon.ac.kr (D.-W. Jeong).

<https://doi.org/10.1016/j.apcatb.2019.02.036>

Received 18 October 2018; Received in revised form 4 February 2019; Accepted 14 February 2019

Available online 15 February 2019

0926-3373/© 2019 Elsevier B.V. All rights reserved.

elements [15–18]. Thus, the development of a Cr-free HT-WGS catalyst with activity exceeding that of the conventional catalyst is a matter of great significance.

Fe-based materials have traditionally been utilized as catalysts for the HT-WGS reaction [19]. Although Fe_3O_4 can catalyze the HT-WGS reaction, promoter-free Fe catalysts suffer from rapid sintering, which is accompanied by a decrease of surface area and loss of activity. Hence, Cr_2O_3 is typically added as a promoter to improve the activity and stability of Fe-based catalysts. Since discovery of the Fe-Cr formulation in 1912 [20], Cr_2O_3 has been widely reported to function as either a textural promoter that stabilizes the surface area of Fe_3O_4 and/or as a structural promoter that enhances $\text{Fe}^{2+} \leftrightarrow \text{Fe}^{3+}$ redox cycling [21–25]. Thus, even though its exact role is still debated, Cr is well known to effectively promote the HT-WGS reaction [21–25]. However, hexavalent chromium (Cr^{VI}) was reported to be a potent carcinogen posing a serious threat to human life and the environment by the U.S. Environmental Protection Agency and the U.S. Occupational Health and Safety Organization reported [26,27], which inspired an ongoing search for methods of substituting Cr in HT-WGS catalysts for other elements [28–32]. Recently, Fe-Al-Cu catalysts have been reported to exhibit outstanding performance in the HT-WGS reaction [33–36], and a number of attempts have been made to demonstrate the possibility of using these catalysts to replace the commercial Fe-Cr catalyst. In the above catalysts, Al acts as a textural promoter that avoids/delays the sintering of active Fe species [11,12,21,31], and the incorporation of Al into the Fe-based catalytic system is additionally favored by the similarity of Fe^{3+} (0.690 Å) and Al^{3+} (0.675 Å) ionic radii. Cu is known to function as a structural promoter that provides new active sites for the WGS reaction and enhances the redox cycling of Fe-based catalysts via the hydrogen spillover effect [37–39]. In previous studies, we have solely tried to optimize the performance of Fe-based catalysts for the conversion of waste-derived synthesis gas [40,41]. However, even for well-developed and optimized catalysts, the catalyst performance gap observed in a scale-up scenario is commonly viewed as a major hurdle for commercial applications [42]. In particular, the scaled-up production of Fe-Al-Cu catalysts for the HT-WGS reaction of waste-derived synthesis gas has not been reported yet, which necessitates the identification of major factors that affect such upscaled syntheses and should therefore be controlled to maintain the characteristics and catalytic performance of the catalyst synthesized on a large scale.

Herein, we aimed to synthesize a highly active and stable Cr-free catalyst for the conversion of waste-derived synthesis gas while avoiding performance degradation and property changes in the case of upscaled production. Specifically, we used a homogeneous co-precipitation method to scale up the synthesis of a Fe-Al-Cu catalyst previously prepared on a laboratory scale and exhibiting excellent performance in the HT-WGS reaction. The physicochemical properties of catalysts prepared on both laboratory and large scales were examined by Brunauer-Emmett-Teller (BET) surface area measurements, pore size distribution analysis, X-ray diffraction (XRD), transmission electron microscopy (TEM), selected area electron diffraction (SAED), X-ray photoelectron spectroscopy (XPS), X-ray absorption near edge structure (XANES), extended X-ray absorption fine structure (EXAFS) and H_2 temperature-programmed reduction (H_2 -TPR), and the above catalysts were compared with each other and with the commercial Fe-Cr catalyst in terms of laboratory-scale HT-WGS reaction performance.

2. Experimental

2.1. Catalyst preparation

Fe-Al-Cu catalysts were synthesized by the homogeneous one-step co-precipitation method. $\text{Fe}(\text{NO}_3)_3 \cdot 9\text{H}_2\text{O}$ (98%, Aldrich), $\text{Al}(\text{NO}_3)_3 \cdot 9\text{H}_2\text{O}$ (98%, Aldrich) and $\text{Cu}(\text{NO}_3)_2 \cdot x\text{H}_2\text{O}$ (99%, Aldrich) were used as precursors. K_2CO_3 (99%, Aldrich) was utilized as the precipitation agent. The loadings of Fe, Al and Cu were fixed at 83, 7 and 10 wt%, respectively. Stoichiometric quantities of precursors were dissolved in

250 mL of distilled water, and a solution of a stoichiometric amount of K_2CO_3 in 250 mL of distilled water was dropwise added into the above precursor solution at 70 °C upon constant stirring. The precipitate was collected by filtration through filter paper (Cat. No. 1005-110, Whatman), washed several times with distilled water, dried in air at 100 °C for 12 h, and finally calcined in air at 400 °C for 3 h to obtain the catalyst. For laboratory-scale synthesis, the concentration of precursor solutions in a fixed volume of distilled water (500 mL) was systematically varied (Fe: 0.042–0.42 M, Al: 0.005–0.05 M, Cu: 0.005–0.05 M), and the obtained catalysts were denoted as FAC-PC-*n*, where *n* equals 1–10 and represents the concentration increase factor, with *n* = 1 corresponding to Fe: 0.042 M, Al: 0.005 M, and Cu: 0.005 M, and *n* = 10 corresponding to Fe: 0.42 M, Al: 0.05 M, and Cu: 0.05 M. For large-scale synthesis, Fe, Al, and Cu precursor concentrations were fixed at 0.126, 0.015, and 0.015 M, respectively. The precursors and K_2CO_3 were dissolved in 10 L of distilled water, so that the total volume of the reaction mixture equaled 20 L, and the procedure used for the laboratory-scale synthesis was applied. Bare Fe and Fe-Al catalysts were prepared as the references. The precipitation and calcination of the bare Fe and Fe-Al catalysts were conducted with the same procedure of the Fe-Al-Cu catalysts. The loading and precursor concentration of Fe for the bare Fe catalyst were 100 wt% and Fe: 0.0051 M (*n* = 1), respectively. The loadings of Fe and Al for the Fe-Al catalyst were fixed at 93 and 7 wt%, respectively, and the precursor concentrations of Fe and Al were Fe: 0.0047 M and Al: 0.005 M (*n* = 1).

2.2. Characterization

N_2 adsorption measurements at −196 °C (ASAP 2010, Micromeritics) were used to determine BET surface areas of fresh samples. Prior to analysis, fresh samples were dried at 110 °C and stored under vacuum overnight. Pore size distributions were determined based on the desorption branch of the N_2 isotherm. XRD patterns were recorded using an X-ray diffractometer (XPRT-PRO, Cu-K α radiation, 40 kV, 30 mA). Fresh and reduced samples were subjected to a wide-range scan performed for $2\theta = 20\text{--}80^\circ$ in steps of $0.02^\circ \text{ s}^{-1}$. Fresh samples were activated in 2 vol % H_2/N_2 at 400 °C for 1 h. The crystallite size of Fe_3O_4 was estimated by applying the Scherrer equation to the peak at 35.4° . TEM images and SAED patterns of the prepared catalysts were obtained using a JEM-F200 (JEOL) microscope with 200 kV operating voltage. All the samples were suspended in ethanol by ultra-sonication, and the prepared suspension was deposited on a copper grid with a carbon film for TEM measurement. XPS spectra were recorded using a Al-K α spectrophotometer (Thermo-Scientific) equipped with a high-resolution monochromator. Survey and detailed spectra of reduced samples were recorded at pass energies of 100 and 50 eV, respectively. Binding energies were adjusted using the C 1s transition at 284.6 eV. Fe K-edge XANES and EXAFS experiments were performed at the 8C Nano XAFS beamline of the Pohang Accelerator Laboratory (PAL), Republic of Korea. XANES and EXAFS spectra of fresh samples were collected in the transmission mode. The data were extracted using Athena and Artemis software (Demeter) with the FEFF8 code. The raw data were smoothed, background-corrected, normalized, and fitted in the *k* range from 3 to 12.9 using the first shell theoretical scattering amplitudes. The fitting results of EXAFS spectra was obtained using the single shell model which is less model dependent and applicable to comparison with any compounds [43,44]. The dispersion of Cu was analyzed by N_2O titration using an Autochem 2920 instrument (Micromeritics). Fresh samples were reduced in 2 vol% H_2/Ar at 400 °C for 1 h. The amount of consumed N_2O was measured by the amount of formed N_2 at 50 °C using a N_2O pulse. The dispersion of Cu was estimated by assuming the stoichiometry of 2 to give the number of copper atoms exposed on the surface per N_2O molecule. TPR patterns were analyzed using an Autochem 2920 instrument (Micromeritics). Full-range TPR experiments were conducted for fresh samples in 10 vol% H_2/Ar at a heating rate of $10^\circ\text{C min}^{-1}$ from 50 to 1000 °C. Mössbauer spectra were recorded using a Mössbauer spectrometer with ^{57}Co γ -ray

source. All spectra were taken at room temperature and ambient atmosphere. The integrated areas of deconvoluted peaks were used to obtain the relative portion of the different Fe species.

2.3. Catalytic reaction

The HT-WGS reaction was carried out at atmospheric pressure in a fixed-bed microtubular quartz reactor with an inner diameter of 4 mm. The reaction temperature was measured and controlled by a K-type thermocouple inserted directly into the middle of the catalyst bed. Prior to the experiment, a 90 mg sample was charged into the middle of the quartz reactor, and inert quartz wool was used to hold the catalyst bed in a fixed position. Before each measurement, the sample was reduced *in situ* in a flow of 2 vol% H₂/N₂ at 400 °C for 1 h. The simulated waste-derived synthesis gas was obtained from the IAE waste gasifier, as reported in a previous study, and comprised 38.2 vol% CO, 21.5 vol% CO₂, 2.3 vol% CH₄, 29.2 vol% H₂, and 8.8 vol% N₂ [11,12]. A mass flow controller (Brooks 5850E) was used for gas feeding, and steam feeding was performed using a syringe pump. For vaporizing water, a heating coil was wrapped around the gas-feeding line before it entered the quartz reactor, and vaporization was performed at 180 °C. The outlet gases were chilled to condense residual water and analyzed on-line using a micro gas chromatograph (Agilent 3000). Activity testing was carried out at 350–550 °C, and sample evaluation was performed at a gas hourly space velocity (GHSV) of 40,057 mL·g⁻¹·h⁻¹ at STP. N₂ was utilized as a reference gas to calculate the conversion, selectivity, and carbon balance, which were defined as:

$$\text{CO conversion (\%)} = \frac{[\text{CO}]_{\text{in}}/[\text{N}_2]_{\text{in}} - [\text{CO}]_{\text{out}}/[\text{N}_2]_{\text{out}}}{[\text{CO}]_{\text{in}}/[\text{N}_2]_{\text{in}}} \times 100$$

$$\text{CO}_2 \text{ selectivity (\%)} = \frac{[\text{CO}_2]_{\text{out}}/[\text{N}_2]_{\text{out}} - [\text{CO}_2]_{\text{in}}/[\text{N}_2]_{\text{in}}}{([\text{CH}_4]_{\text{out}}/[\text{N}_2]_{\text{out}} - [\text{CH}_4]_{\text{in}}/[\text{N}_2]_{\text{in}}) + ([\text{CO}_2]_{\text{out}}/[\text{N}_2]_{\text{out}} - [\text{CO}_2]_{\text{in}}/[\text{N}_2]_{\text{in}})} \times 100$$

$$\text{CH}_4 \text{ selectivity (\%)} = \frac{[\text{CH}_4]_{\text{out}}/[\text{N}_2]_{\text{out}} - [\text{CH}_4]_{\text{in}}/[\text{N}_2]_{\text{in}}}{([\text{CH}_4]_{\text{out}}/[\text{N}_2]_{\text{out}} - [\text{CH}_4]_{\text{in}}/[\text{N}_2]_{\text{in}}) + ([\text{CO}_2]_{\text{out}}/[\text{N}_2]_{\text{out}} - [\text{CO}_2]_{\text{in}}/[\text{N}_2]_{\text{in}})} \times 100$$

$$\text{Carbon balance (\%)} = \frac{([\text{CH}_4]_{\text{out}} + [\text{CO}]_{\text{out}} + [\text{CO}_2]_{\text{out}})/[\text{N}_2]_{\text{out}}}{([\text{CH}_4]_{\text{in}} + [\text{CO}]_{\text{in}} + [\text{CO}_2]_{\text{in}})/[\text{N}_2]_{\text{in}}} \times 100$$

where the subscripts “in” and “out” refer to inlet and outlet concentrations, respectively.

Turnover frequency (TOF) was calculated using the following equation,

$$\text{TOF} = \frac{(\text{CO}_{\text{in}} - \text{CO}_{\text{out}}) \text{AB}_M F}{D_M W X_M}$$

Where CO_{in} and CO_{out} are the inlet and outlet concentrations of CO, respectively; AB_M is the atomic weight of active metal; F is the total flow rate (mol·s⁻¹); D_M is the dispersion; W is the mass of catalyst (g_{cat}); and X_M is the metal content (g_M·g_{cat}⁻¹).

3. Results and discussion

Scheme 1 summarizes the research progress on Cr-free Fe-Al-Cu catalysts described in previous works. Specifically, our group has extensively investigated Fe-based catalysts to improve their performance for the conversion of waste-derived synthesis gas, screening a number of additives for the target reaction [11,12,40,41]. As a result, we developed a promising Fe-Al-Cu catalyst and demonstrated the promotional role of Al and Cu, additionally elucidating the optimum composition (Fe: 83 wt%, Al: 7 wt%, Cu: 10 wt%) and demonstrating the superiority of the catalyst prepared by co-precipitation under optimized conditions [11,12,40,41]. Herein, we demonstrate the applicability of the previously developed catalyst preparation method to large-scale production, showing the importance of choosing suitable precursor concentrations for physicochemical property and catalytic performance preservation. Catalysts prepared using various precursor

concentrations were synthesized on the laboratory scale in a 0.5 L reactor, and the weight of obtained samples was obtained after the catalyst synthesis procedure, as summarized in Table 1. For large-scale production, precursor concentrations were chosen in such a way as to minimize the extent of performance degradation and simultaneously maximize the amount of the produced catalyst. Large-scale synthesis was performed in a 20 L reactor (laboratory scale × 40) and afforded 224 g of the catalyst (FAC-PC-3-240; 93% yield). This amount of the catalysts was required to operate the HT-WGS reactor of 1.0 Nm³·h⁻¹.

3.1. Catalyst characterization

3.1.1. Laboratory-scale fresh catalysts (FAC-PC-1 ~ FAC-PC-10)

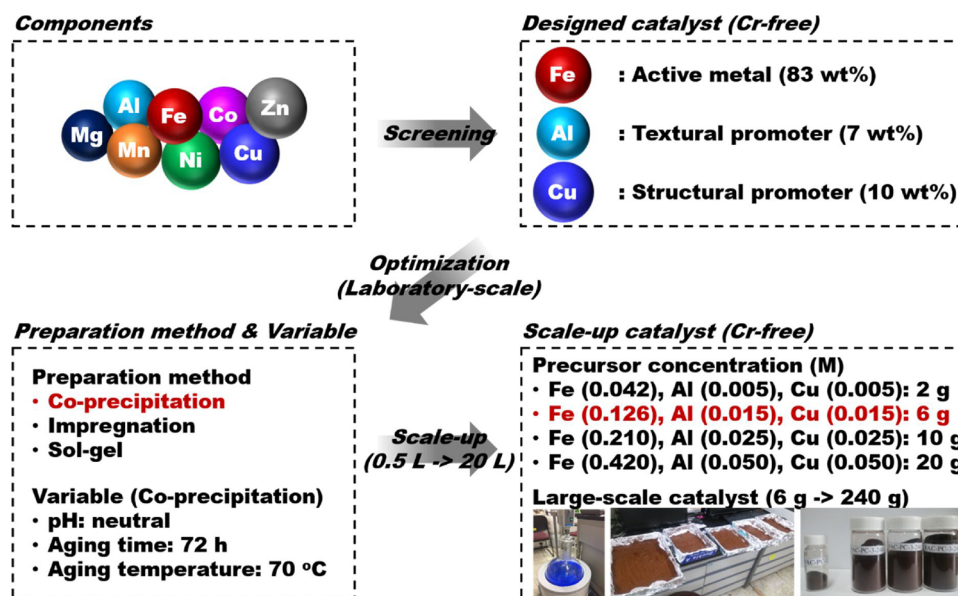
Table 1 summarizes the BET surface areas of as-prepared catalysts, demonstrating that FAC-PC-1 and FAC-PC-3 exhibited almost identical values of 168 and 165 m²·g⁻¹, respectively. In the case of FAC-PC-5, the BET surface area decreased to 132 m²·g⁻¹, and the lowest surface area of 60 m²·g⁻¹ was observed for FAC-PC-10.

Fig. S1 shows that the studied catalysts featured type V (as classified by the International Union of Pure and Applied Chemistry) N₂ adsorption/desorption isotherms with different hysteresis patterns, which indicated the presence of pores [45]. The N₂ isotherms of FAC-PC-1 and FAC-PC-3 featured type H2 hysteresis, which was attributed to disordered porosity featuring interconnections between adjacent pores. Conversely, FAC-PC-5 and FAC-PC-10 featured type H3 and H4 hysteresis, respectively. Hysteresis of these two types does not correspond to any well-defined pore structure, but is typically observed for complex materials containing both meso- and micropores. Fig. S2 shows pore size distributions estimated from the N₂ desorption branch using the BJH method, revealing that FAC-PC-1 and FAC-PC-3 featured pores with uniform diameters of 4.2 and 4.9 nm, respectively. Notably, the development of micropores was observed starting from *n* = 5, e.g., FAC-PC-5 contained pores with diameters of 4.6 and 3.5 nm, whereas FAC-PC-10 contained primary and secondary pores with diameters of 3.4 and 4.2 nm, respectively. These results confirmed that FAC-PC-1 and FAC-PC-5 contained homogeneous uniform pores and exhibited high surface areas.

Fig. 1 shows that the XRD patterns of all fresh catalysts did not contain any sharp peaks, even though these catalysts had been calcined at 400 °C. This low degree of crystallinity was attributed to the formation of amorphous mixed oxide phases, namely α-Fe₂O₃ (hematite, JCPDS #33-0664) and γ-Fe₂O₃ (maghemite, JCPDS #39-1346) [21]. Typically, calcined fresh Fe-based catalysts show well-defined peaks of crystalline α-Fe₂O₃ [11,12,33], as observed for bare Fe and Fe-Al catalysts (Fig. S3), whereas as-prepared Fe-Al-Cu catalysts exhibited a diffraction peak of γ-Fe₂O₃ at 35.63° [21,33,34,46,47]. α-Fe₂O₃ possesses a hexagonal structure containing fully oxidized Fe³⁺ ions, while γ-Fe₂O₃ has an imperfect spinel structure that can be represented as [Fe₈³⁺]^{tetra}[Fe_{40/3}³⁺□_{8/3}]^{octa}O₃₂ [21,33,34,46,47], where tetra, octa, and □ correspond to tetrahedral, octahedral, and vacant cation sites, respectively.

The morphology of the prepared catalysts, bare Fe and Fe-Al was analyzed by TEM and the result images are shown in Fig. S4. The particle size of both bare Fe and Fe-Al was ca. 50 nm, while those of the prepared catalysts were a range from 10 to 20 nm. It is obvious that the particle size of the prepared catalysts is smaller than those of bare Fe and Fe-Al. Furthermore, FAC-PC-1 and FAC-PC-3 showed a uniform particle. FAC-PC-5 contained the particle with a size of 23.6 nm, but it was more uniform compared to FAC-PC-10. This result is in good agreement with BET result. The high-resolution TEM images and SAED patterns of FAC-PC-3, FAC-PC-3-240 and Fe-Al are shown in Fig. 2. SAED pattern of Fe-Al showed (110), (113), (202) and (116) planes, which are assigned to the α-Fe₂O₃ (JCPDS #33-0664). On the contrary, FAC-PC-3 showed (311) and (440) planes, which are ascribed to the γ-Fe₂O₃ (JCPDS #39-1346).

The chemical structure of catalysts was probed by XPS, with Fe 2p and Cu 2p spectra provided in Figs. S5(a) and (b), respectively. Notably, the former spectra were split into two peaks because of spin-orbit coupling (Fe 2p_{1/2} and Fe 2p_{3/2}). Based on previous studies, the main



Scheme 1. Research progress on Cr-free Fe-Al-Cu catalysts reported in previous works.

Table 1
Properties of the prepared Fe-Al-Cu catalysts.

Catalyst	Precursor concentration (M)			Weight of obtained sample (g)	BET surface area (m ² /g) ^a	Fe ₃ O ₄ crystallite size (nm) ^b	Cu dispersion (%) ^c	TOF (s ⁻¹) ^d
	Fe	Al	Cu					
FAC-PC-1	0.042	0.005	0.005	2	168	13.4	5.9	0.77
FAC-PC-3	0.126	0.015	0.015	6	165	13.7	5.7	0.80
FAC-PC-5	0.210	0.025	0.025	10	132	16.6	4.7	0.86
FAC-PC-10	0.420	0.050	0.050	20	60	22.3	2.8	0.85
FAC-PC-3-240	0.126	0.015	0.015	240	166	15.9	5.6	0.81

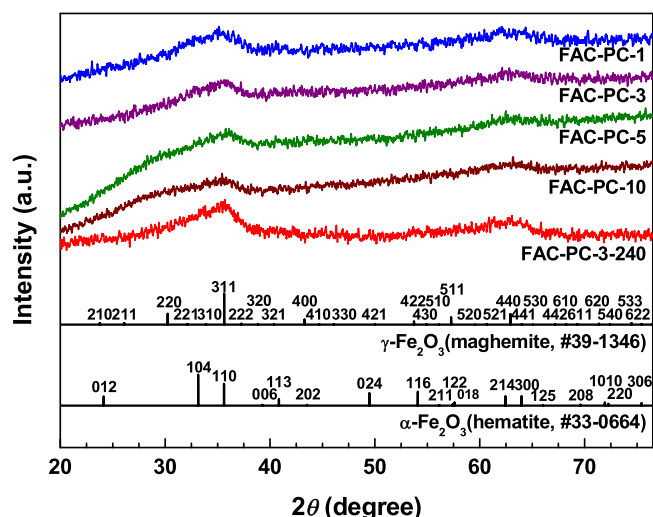
^a Estimated from the N₂ adsorption isotherm at −196 °C.^b Estimated from the Fe₃O₄ (311) XRD peak at 35.4°.^c Calculated from N₂O titration method.^d T = 350 °C, P = 1 atm, GHSV = 40,057 mL g⁻¹ h⁻¹.

Fig. 1. XRD patterns of fresh Fe-Al-Cu catalysts.

peaks at 710.8 eV could be assigned to Fe³⁺ in either α-Fe₂O₃ or γ-Fe₂O₃. γ-Fe₂O₃ was reported to show a clear narrow peak at 710.8 eV, whereas α-Fe₂O₃ was reported to exhibit two distinct peaks at 709.7 and 710.8 eV [48]. The prepared catalysts showed a major peak at 710.8 eV and no peak at 709.7 eV, indicating that they contain γ-Fe₂O₃.

However, it is hard to distinguish clearly the phase between α-Fe₂O₃ or γ-Fe₂O₃ by XPS. In the case of Cu 2p spectra, all catalysts showed the peak of Cu²⁺ (CuO) at 933.8 eV.

XAS studies were performed to obtain detailed information on the Fe species. Fig. 3 shows the Fe K-edge XANES spectra of the prepared catalysts with α-Fe₂O₃ and Fe₃O₄ as the references. The absorption peaks of pre-edge are observed at ca. 7115 eV. The X-ray absorption of pre-edge in Fe K-edge is responsible for 1s → 3d transition. This transition is forbidden in the octahedral coordination of FeO₆, but it occurs in tetrahedral or distorted octahedral coordination [49–51]. Bare Fe and Fe-Al show similar absorption peaks to that of α-Fe₂O₃, which is consistent with the XRD results. On the contrary, the absorption peaks of pre-edge in the prepared catalysts are more intense compared to that of α-Fe₂O₃. This indicates the existence of Fe³⁺ ions in tetrahedral or distorted octahedral coordination, implying the formation of γ-Fe₂O₃ [49,51]. Likewise, the same trend can be seen in the main absorption peaks of XANES. The absorption peaks of prepared catalysts are shifted toward lower energy compared to those of bare Fe, Fe-Al and α-Fe₂O₃. This shift is owing to the presence of γ-Fe₂O₃, resulting from the distortion of FeO₆ in the α-Fe₂O₃ structure [49,51–57].

Fig. 4 depicts the k²-weighted Fourier transformed (FT) functions obtained from the EXAFS oscillations of bare Fe, Fe-Al, FAC-PC-3 and FAC-PC-3-240. The best fit results are shown in Fig. 4 and the structural and statistical information (coordination number (N), interatomic distance (R), and Debye-Waller factor (σ²)) is summarized in Table 2. Both experimental and fitting results show two peaks, that are assigned to

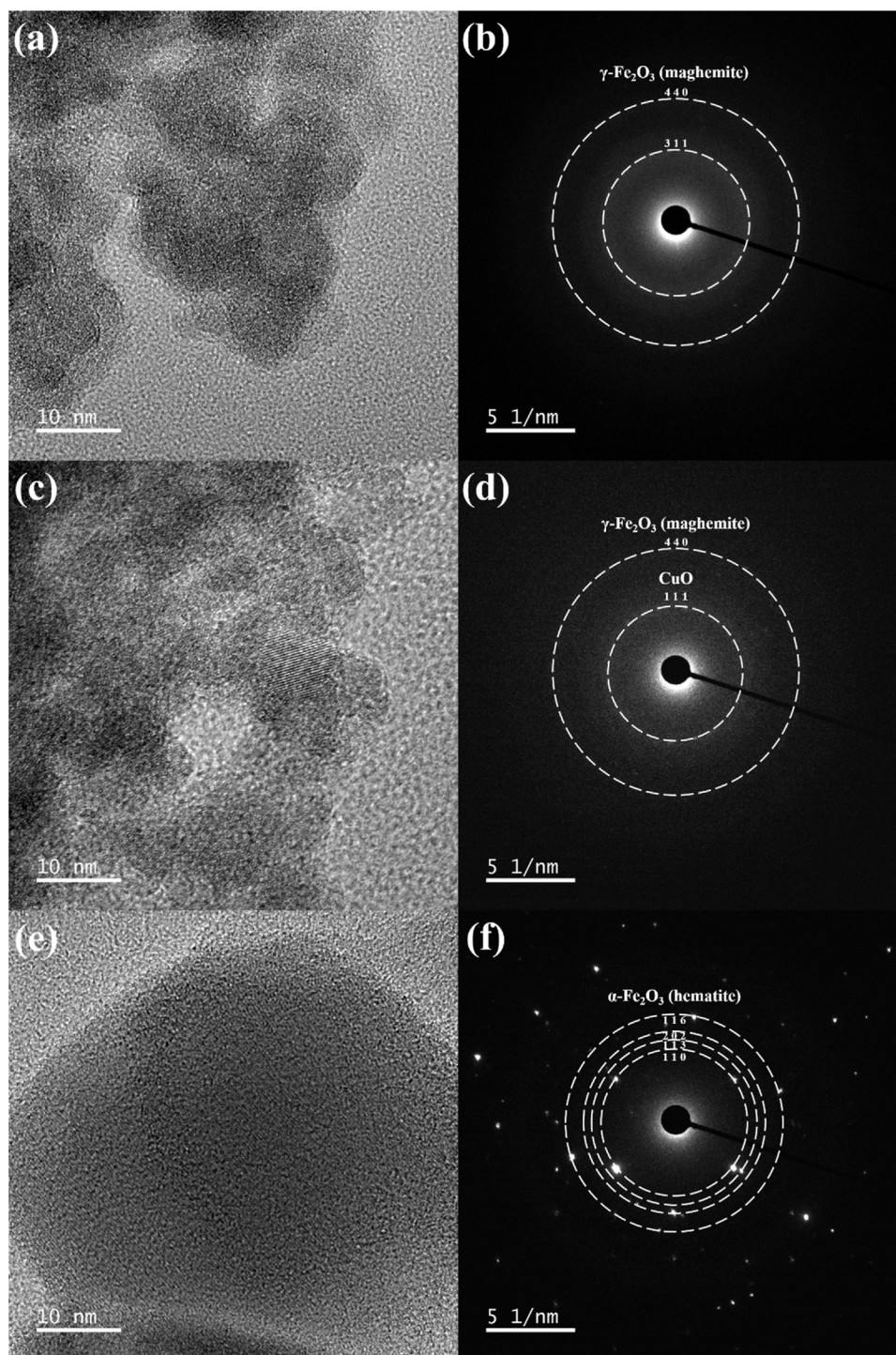


Fig. 2. TEM images and SAED patterns of fresh FAC-PC-3, FAC-PC-3-240 and Fe-Al catalysts: (a) and (b) FAC-PC-3, (c) and (d) FAC-PC-3-240, (e) and (f) SAED Fe-Al.

the Fe-O and Fe-Fe scattering, respectively [58,59]. In general, α -Fe₂O₃ is known to have 6 Fe-O coordination with average distance of 2.05 Å, which is responsible for the Fe-O bond in the octahedral FeO₆ [43,60]. For both bare Fe and Fe-Al, the values of *N* and *R* are similar to those of α -Fe₂O₃, because of their same hematite phase. On the contrary, the Fe-O distance of the prepared catalysts is shorter than those of α -Fe₂O₃. Likewise, the *N* values of Fe-O coordination for the prepared catalysts are lower than those of the bare Fe, Fe-Al and α -Fe₂O₃. This is due to the contribution of lower coordination number and shorter distance of Fe-O in tetrahedral FeO₄ or distorted octahedral coordination, implying the existence of γ -Fe₂O₃, which is not fully oxidized but partially

distorted [43,50,60,61]. These results are in good agreement with the results obtained from XRD, SAED and XANES.

Above results demonstrated the formation of γ -Fe₂O₃, which is significant for the WGS reaction. For the Fe-based catalysts, Fe₃O₄ is well-known for the active phase in the target reaction. It possesses an inverse spinel structure that is represented as [Fe³⁺]_{tetra}[Fe³⁺+Fe²⁺]_{octa}O₄. γ -Fe₂O₃ can be easily transformed into Fe₃O₄ compared to fully oxidized α -Fe₂O₃ containing only octahedral FeO₆. This is due to the structural similarity between γ -Fe₂O₃ and Fe₃O₄, which possess tetrahedral FeO₄ or distortion in octahedral FeO₆ [21,33,34,46,47]. Thus, the prepared catalysts are expected to exhibit easier reducibility that is a key property in

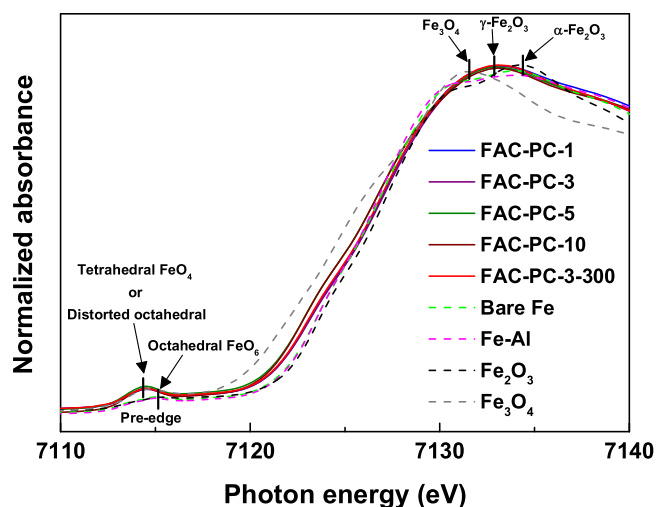


Fig. 3. XANES spectra of fresh Fe-Al-Cu, bare Fe, Fe-Al, α -Fe₂O₃ and Fe₃O₄ catalysts.

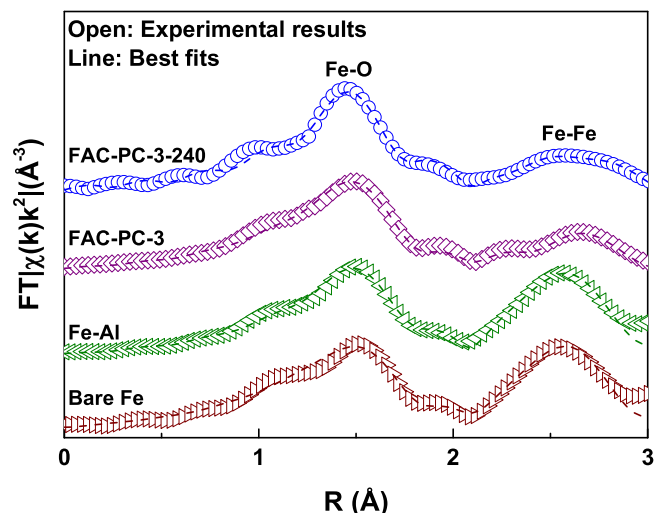


Fig. 4. Best fits of k^2 weighted Fourier-transformed EXAFS spectra over bare Fe, Fe-Al, FAC-PC-3 and FAC-PC-3-240 catalysts.

determining the catalytic performance, being dominated by redox mechanism of the WGS reaction. In addition, the incorporation of Cu into hematite lattice has an important role in improving Cu dispersion, resulting from the anchoring effect. Moreover, this leads to the formation of γ -Fe₂O₃ ([Fe₈³⁺]_{tetra}[Fe_{40/3}³⁺]_{octa}O₃₂) with defect sites, leading higher surface area of the catalysts compared to the bare Fe and Fe-Al. On the other hands, it should be pointed out that the incorporation of both Al and Cu into Fe-based catalysts results in the formation of γ -Fe₂O₃ [34,41,46], the extent of which is known to be significantly dependent on the preparation method [33,41]. Sol-gel and co-precipitation methods have been shown to afford a uniform distribution of promoters and hence

result in the formation of the γ -Fe₂O₃ phase [33,41]. Thus, the co-precipitation method used in this study was concluded to result in the formation of γ -Fe₂O₃ and the homogeneous incorporation of Cu and Al.

3.1.2. Laboratory-scale activated catalysts (FAC-PC-1 ~ FAC-PC-10)

To confirm the formation of the active phase (Fe₃O₄), catalysts subjected to 1 h *ex situ* activation at 400 °C with 2 vol% H₂/N₂ and overnight room-temperature passivation with 2 vol% O₂/N₂ were probed by XRD (Fig. 5). Diffraction peaks at 30.1, 35.4, 37.1, 43.1, 53.4, 56.9, 62.5, 73.9, and 75.0° observed in all cases were assigned to Fe₃O₄ (magnetite, JCPDS #65-3107), and the prominent peak at 44.7° was attributed to metallic Fe (JCPDS #65-4899) produced by the reduction of Fe₃O₄ [34]. The sizes of Fe₃O₄ crystallites were calculated by applying the Scherrer equation to the Fe₃O₄ (311) peak at 35.4° and are summarized in Table 1. Among the prepared catalysts, FAC-PC-1 exhibited the smallest crystallite size of 13.4 nm, while FAC-PC-10 exhibited the largest size of 22.3 nm. Interestingly, FAC-PC-1 and FAC-PC-3 showed very similar crystallite sizes. Moreover, the crystallite size dramatically increased with increasing precursor concentration for $n > 5$. The trend observed for the crystallite size of activated catalysts was well matched with that of BET surface areas of fresh catalysts, which revealed that the crystallite size of activated catalysts is possibly affected by the properties of fresh catalysts. In order to identify clearly the effect of precursor concentration on the size of catalysts, Cu dispersion of the prepared catalysts were analyzed. In the case of the Fe dispersion, it is hard to estimate the dispersion of Fe under the condition of the activation at 400 °C with 2 vol % H₂/N₂ for 1 h. Thus, Cu dispersion by N₂O titration were estimated and summarized in Table 1. The trend of Cu dispersion is clearly consistent with that of the crystallite size. Cu dispersion decreased with increasing precursor concentration.

Detailed information on reduction processes occurring during activation was obtained by TPR. Fig. S6 shows the full-temperature-range (50–1000 °C) TPR patterns of the investigated catalysts, revealing the presence of sharp peaks at low temperatures and broad peaks at high temperatures, which were ascribed to the reduction of CuO and γ -Fe₂O₃ [21,33,34] and to the reduction of Fe₃O₄ to FeO or metallic Fe° [62–64], respectively. The above reduction pattern was clearly distinct from that of bare Fe, which features three peaks at 405, 700, and 950 °C corresponding to the reduction of α -Fe₂O₃ to Fe₃O₄, Fe₃O₄ to FeO, and FeO to Fe°, respectively (Fig. S7) [11,12,62–64]. It should be pointed out that the first reduction peak of FAC catalysts was shifted to lower temperature relative to that of bare Fe, which indicated that the presence of both Al and Cu facilitates the formation of the Fe₃O₄ active phase. This finding agreed with the reduction behavior of Cu-promoted γ -Fe₂O₃, which is known to be easily activated [21,33,34,46,47]. The low-temperature peaks could be deconvoluted into two sub-peaks corresponding to the reduction of CuO to Cu° and to that of γ -Fe₂O₃ (Fig. 6) [34,39]. Notably, both of the above peaks were observed at a significantly lower temperature for FAC-PC-1 and FAC-PC-3, whereas the highest reduction temperature was observed for FAC-PC-10. Thus, the reduction behavior of the prepared catalysts was influenced by precursor concentration, even though the major Fe-containing species contained therein was the easily reducible Cu-promoted γ -Fe₂O₃, which demonstrated the strong influence of support/promoter type on catalyst reducibility. Additionally, one needs to consider that small particles and

Table 2

Structural and statistical parameters of bare Fe, Fe-Al, FAC-PC-3 and FAC-PC-3-240 catalysts.

Description	Scattering path: Fe-O			Scattering path: Fe-Fe		
	N	R (Å)	σ^2 (Å ² × 10 ⁻³)	N	R (Å)	σ^2 (Å ² × 10 ⁻³)
Bare Fe	5.9	2.03 ± 0.02	3.7 ± 2.1	2.3	2.94 ± 0.01	1.0 ± 1.7
Fe-Al	5.9	2.04 ± 0.02	3.7 ± 1.2	2.2	2.94 ± 0.01	0.5 ± 1.5
FAC-PC-3	5.0	2.02 ± 0.01	4.8 ± 1.4	1.5	2.93 ± 0.02	7.3 ± 2.0
FAC-PC-3-240	4.7	2.01 ± 0.01	0.4 ± 0.8	1.6	2.99 ± 0.02	2.5 ± 2.3

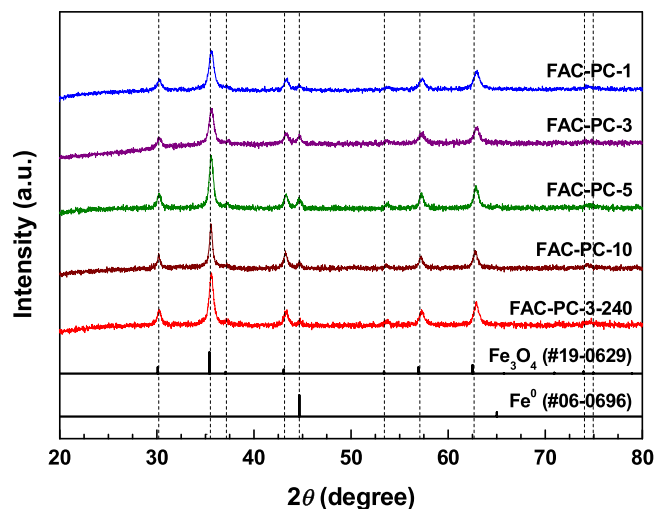


Fig. 5. XRD patterns of activated Fe-Al-Cu catalysts.

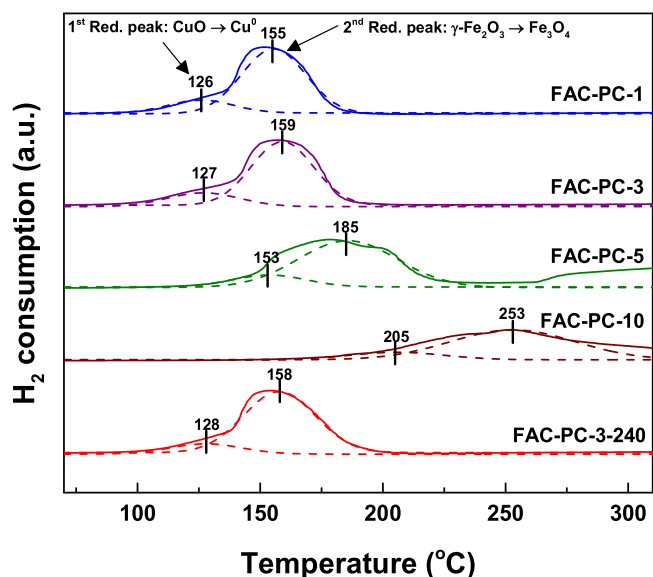


Fig. 6. Deconvoluted TPR patterns of fresh Fe-Al-Cu catalysts.

highly dispersed metal on the catalyst surface are reduced easier than large particles in the bulk. Herein, surface area, particle size and dispersion were viewed as possibly important factors influencing catalyst reducibility, since all catalysts were prepared using identical precursor ratios and experimental procedures. As a result, both FAC-PC-1 and FAC-PC-3 were concluded to possess enhanced reducibility and were therefore expected to exhibit superior catalytic performance in the HT-WGS reaction.

3.1.3. Large-scale fresh and activated catalysts (FAC-PC-3-240)

Fresh and activated FAC-PC-3-240 catalysts were prepared in the large-scale reactor using precursor concentrations identical to those used for the synthesis of FAC-PC-3 and exhibited a BET surface area ($166 \text{ m}^2 \text{ g}^{-1}$) similar to that of the latter catalyst (Table 1). Likewise, the corresponding isotherm curves (type V with H_2 hysteresis) were also similar (Fig. S1). Although the pore size distribution of FAC-PC-3-240 was broader than that of FAC-PC-3, it remained homogenous, in contrast to the cases of FAC-PC-5 or FAC-PC-10 (Fig. S2). Fresh FAC-PC-3-240 was shown to contain $\gamma\text{-Fe}_2\text{O}_3$ by XRD (Fig. 1), SAED (Fig. 2), XANES (Fig. 3) and EXAFS (Fig. 4) analyses. In general, $\alpha\text{-Fe}_2\text{O}_3$ is known to have 6 Fe-O coordination with average distance of 2.05 \AA , which is responsible for the Fe-O bond in the octahedral FeO_6 [43,60].

For both bare Fe and Fe-Al, the values of N and R are similar to those of $\alpha\text{-Fe}_2\text{O}_3$, because of their same hematite phase. On the contrary, the Fe-O distance of the prepared catalysts is shorter than those of $\alpha\text{-Fe}_2\text{O}_3$. Likewise, the N values of Fe-O coordination for the prepared catalysts are lower than those of the bare Fe, Fe-Al and $\alpha\text{-Fe}_2\text{O}_3$. In order to confirm clearly the presence of $\gamma\text{-Fe}_2\text{O}_3$ on the catalysts prepared in the large-scale, Mössbauer spectroscopy was analyzed. Mössbauer spectroscopy has been well-known for a powerful tool to identify the underlying aspects of Fe local structure [33,64]. Fig. 7 shows the Mössbauer spectra of bare Fe and FAC-PC-3-240. Spectra were fitted using sextets and doublets. In general, the Mössbauer spectrum of Fe consist of sextet and doublet which are ascribed to the $\alpha\text{-Fe}_2\text{O}_3$ and $\gamma\text{-Fe}_2\text{O}_3$, respectively [33,64]. This reflects that $\alpha\text{-Fe}_2\text{O}_3$ is dominant in bare Fe whereas $\gamma\text{-Fe}_2\text{O}_3$ is dominant in FAC-PC-3-240. The XRD pattern of activated FAC-PC-3-240 (Fig. 5) indicated the formation of the Fe_3O_4 active phase, the crystallite size (15.9 nm) of which slightly exceeded that observed for FAC-PC-1 (13.7 nm). The TPR curve of FAC-PC-3-240 (Fig. 6) featured two reduction peaks at 128 and 158°C , signifying a reducibility comparable to that of FAC-PC-3. Thus, the above findings demonstrated that the key catalyst characteristics could be well maintained by controlling precursor concentration even in the case of a scaled-up ($\times 40$) production.

3.2. Catalytic performance of the Cr-free FAC catalysts

3.2.1. HT-WGS activity of the FAC catalysts (FAC-PC-1 ~ FAC-PC-10)

The prepared catalysts were used to promote the HT-WGS reaction at a $\text{H}_2\text{O}/(\text{CH}_4 + \text{CO} + \text{CO}_2)$ ratio of 2.0 and a GHSV of $40,057 \text{ mL g}^{-1} \text{ h}^{-1}$ after 1 h *in situ* activation in 2 vol% H_2/N_2 at 400°C . Fig. S8 shows the dry-basis compositions of influent and effluent gases for the HT-WGS reaction over FAC-PC-1, revealing that the latter contained less CO and more H_2 and CO_2 and thus indicating the conversion of $\text{CO} + \text{H}_2\text{O}$ into $\text{H}_2 + \text{CO}_2$.

Fig. 8 shows CO conversion as a function of reaction temperature ($350\text{--}550^\circ\text{C}$), revealing that at 350°C , conversions of 94.9 and 95.4% were observed for FAC-PC-1 and FAC-PC-3, respectively. Notably, CO conversion decreased to 84.6% in the case of FAC-PC-5, and a minimum of 54.3% was observed for FAC-PC-10. FAC-PC-1 and FAC-PC-3 catalysts showed excellent CO conversion within the whole temperature range, whereas FAC-PC-5 and FAC-PC-10 achieved maximum CO conversions of 86.5% (400°C) and 83.6% (450°C), respectively. Thus, the activity of the above catalysts was determined to follow the order of

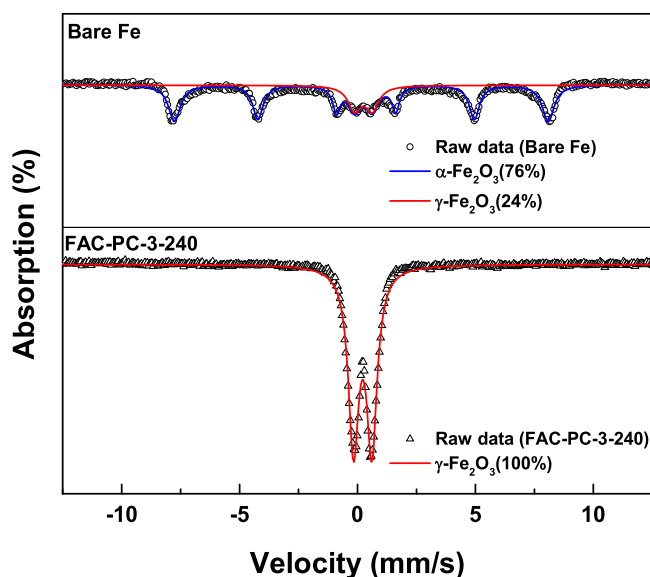


Fig. 7. Mössbauer spectra and best fits of bare Fe and FAC-PC-3-240.

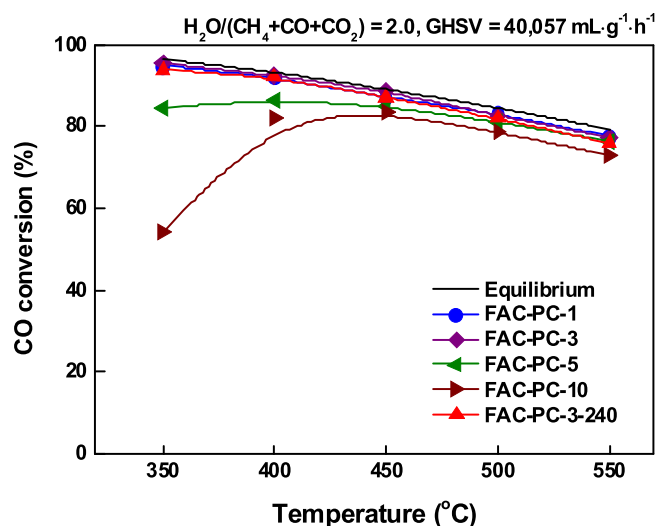


Fig. 8. CO conversion over Fe-Al-Cu catalysts as a function of reaction temperature ($\text{H}_2\text{O}/(\text{CH}_4 + \text{CO} + \text{CO}_2) = 2.0$; $\text{GHSV} = 40,057 \text{ mL}\cdot\text{g}^{-1}\cdot\text{h}^{-1}$).

FAC-PC-1 \approx FAC-PC-3 > FAC-PC-5 > FAC-PC-10. On the other hand, the decrease of CO conversion with increasing reaction temperature was attributed to the equilibrium limitation caused by the exothermic nature of the WGS reaction.

Carbon balance and selectivity were calculated to monitor undesirable side reactions, e.g., C_2 + hydrocarbon production (Table S1). Specifically, the carbon balance was estimated by comparing the amounts of carbon in the influent and effluent gases and equaled $100 \pm 2\%$ for all catalysts, which was within the experimental error. Thus, the HT-WGS reaction was concluded to proceed without the formation of undesirable liquid products or carbonate species. The occurrence of the gas-phase catalytic reaction was confirmed by determining the selectivities of CO_2 (WGS) and CH_4 (methanation, $\text{CO} + 3\text{H}_2 \rightleftharpoons \text{CH}_4 + \text{H}_2\text{O}$ or $\text{CO}_2 + 4\text{H}_2 \rightleftharpoons \text{CH}_4 + 2\text{H}_2\text{O}$) formation (Fig. S9). The prepared catalysts showed reaction temperature-independent CO_2 selectivities of almost 100% and could therefore selectively convert $\text{CO} + \text{H}_2\text{O}$ into $\text{CO}_2 + \text{H}_2$ without promoting the hydrogen-consuming methanation reaction [65,66].

3.2.2. Correlation between characteristics and catalytic performance

The physicochemical properties of the prepared catalysts were compared with their performances in the HT-WGS reaction (Fig. 9 and Table 1). First, BET surface area, Fe_3O_4 crystallite size, reducibility, and Cu dispersion were chosen as key properties, since they are known to affect the abovementioned catalytic performance [16,18,28,29,35,57–59]. FAC-PC-1 and FAC-PC-3 showed the highest BET surface area, smallest Fe_3O_4 crystallite size, outstanding reducibility, and highest Cu dispersion. On the contrary, FAC-PC-5 and FAC-PC-10 exhibited low BET surface area, large Fe_3O_4 crystallite size, poor reducibility, and low dispersion, and this property combination was therefore concluded to be inappropriate for obtaining excellent catalytic performance. The fact that FAC-PC-1 and FAC-PC-3 showed the highest CO conversion and did not promote undesirable side reactions reveals that the performance of FAC catalysts possibly depends on the BET surface area, crystallite size, reducibility, and Cu dispersion. In particular, the easy reducibility of the above catalysts was believed to facilitate redox cycling during the WGS reaction via rapid electron exchange between Fe^{3+} and Fe^{2+} ions, as confirmed by comparison of bare Fe, Fe-Al, and Fe-Al-Cu catalysts. It was widely accepted that the redox mechanism is dominant for the HT-WGS reaction over Fe-based catalysts [23]. Fe^{2+} was oxidized to Fe^{3+} by H_2O and Fe^{3+} was reduced by CO. It was also found that the catalytic activity depends on the reducibility of $\text{Fe}^{3+} \rightleftharpoons \text{Fe}^{2+}$ redox couple, which is determined by the reducibility of the easier reduction of Fe^{3+} oxide. For the Fe-Al-Cu

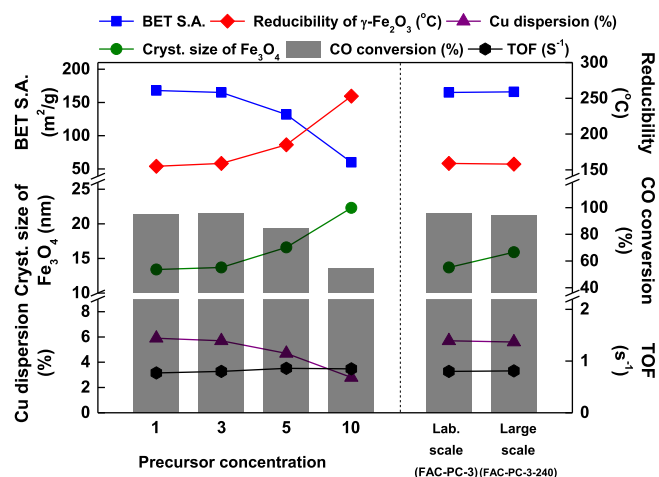


Fig. 9. Correlation between physicochemical properties and HT-WGS reaction performance for catalysts prepared on laboratory and large scales (CO conversion and TOF at 350°C).

catalysts, the incorporation of Cu into hematite (Fe_2O_3) modified the reducibility of Fe^{3+} species. Thus, the higher activity of Fe-Al-Cu catalysts can be explained to be related to the reducibility of catalysts. Fig. S7 depicts the TPR patterns of bare Fe and Fe-Al catalysts, showing that the incorporation of Al did not significantly affect the reducibility of Fe species. As a result, both catalysts achieved similar CO conversions that were clearly lower than that of the Fe-Al-Cu catalyst (Fig. S10). Second, the promotional effect of Cu on increasing the number of additional active site directly influences the catalytic performance. TOF values were estimated by using Cu dispersion and CO conversion at 350°C . Similar TOF values of ca. 0.8 s^{-1} were obtained over the prepared catalysts as a result of that CO conversion was proportional to Cu dispersion. This reveals that FAC-PC-1 and FAC-PC-3 catalysts have larger Cu active sites than FAC-PC-5 and FAC-PC-10 showing poor Cu dispersion, resulting in the high CO conversion FAC-PC-1 and FAC-PC-3. As a consequence, the conversion of CO over the prepared Fe-Al-Cu catalysts was mainly facilitated by the easy reducibility of Fe species and the formation of additional Cu active sites resulting from the promotional effect of Cu.

3.2.3. Possibility of Cr substitution and applicability of large-scale catalysts (FAC-PC-3-240 and commercial Fe-Cr)

In the characterization section, the physicochemical properties of FAC-PC-3-240 were confirmed to be similar to those of FAC-PC-3. Specifically, the BET surface area and reducibility were maintained upon scale-up, while Fe_3O_4 crystallite size slightly increased from 13.5 to 15.9 nm. FAC-PC-3-240 and commercial Fe-Cr (Alfa Aesar) catalysts were applied to the HT-WGS reaction to demonstrate the possibility of substituting the latter for the former. Fig. 10 shows CO conversions achieved over FAC-PC-3-240, FAC-PC-3, and commercial Fe-Cr catalysts, demonstrating that FAC-PC-3-240 achieved high CO conversion similar to that of FAC-PC-3 despite exhibiting an increased Fe_3O_4 crystallite size. At a GHSV of $40,057 \text{ mL}\cdot\text{g}^{-1}\cdot\text{h}^{-1}$, both FAC-PC-3-240 and FAC-PC-3 achieved higher CO conversion than the commercial Fe-Cr catalyst. Conversely, at a GHSV of $3000 \text{ mL}\cdot\text{g}^{-1}\cdot\text{h}^{-1}$, the commercial catalyst achieved equilibrium CO conversion within the temperature range of $400\text{--}550^\circ\text{C}$ (except for 350°C), which indicated that the CO conversion difference observed at $40,057 \text{ mL}\cdot\text{g}^{-1}\cdot\text{h}^{-1}$ was caused by the high CO content of waste-derived synthesis gas. The excellent performance of the prepared Fe-Al-Cu catalysts was ascribed to the promotional effect of Cu on the formation of new active sites for the WGS reaction. The inset of Fig. 10 shows CO conversion as a function of time-on-stream over FAC-PC-3-240 and commercial Fe-Cr catalysts, revealing that whereas both catalysts showed similar stabilities, their activities were markedly different. The obtained activity and stability

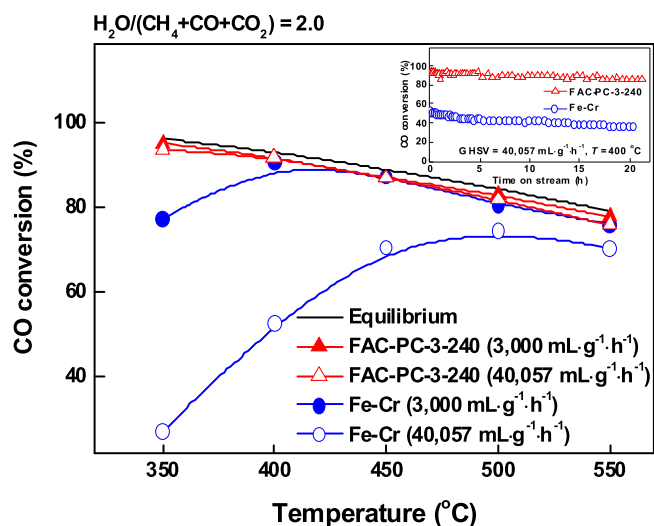


Fig. 10. Temperature-dependent CO conversion over FAC-PC-3-240 and commercial Fe-Cr catalysts at GHSVs of 3000 and 40,057 mL·g⁻¹·h⁻¹ (H₂O/(CH₄ + CO + CO₂) = 2.0). Inset: CO conversion as a function of time-on-stream (H₂O/(CH₄ + CO + CO₂) = 2.0; GHSV = 40,057 mL·g⁻¹·h⁻¹; T = 400 °C).

insights demonstrated that the conversion of waste-derived synthesis gas via the WGS reaction requires the use of catalysts with elevated activity, revealing that the Fe-Al-Cu catalyst exhibits excellent reducibility and is a promising substitute for the commercial Fe-Cr catalyst. Importantly, the properties of the former catalyst were shown to be maintained during large-scale production, which resulted in high activity and stable catalytic performance.

4. Conclusions

Cr-free Fe-Al-Cu catalysts were prepared by homogeneous one-step co-precipitation at various precursor concentrations (Fe: 0.042–0.42 M, Al: 0.005–0.05 M, and Cu: 0.005–0.05 M), and their characteristics and performance were assessed to demonstrate the possibility of replacing Cr-containing catalysts and H₂ production from waste-derived synthesis gas. Whereas all Cu-promoted catalysts were shown to contain γ-Fe₂O₃, which could be more easily transformed into Fe₃O₄ than α-Fe₂O₃ in view of structural similarity considerations, the BET surface area, Fe₃O₄ crystallite size, reducibility, and Cu dispersion of these catalysts strongly depended on precursor concentration. FAC-PC-1 and FAC-PC-3 achieved higher CO conversions in the WGS reaction than other catalysts and did not promote undesirable side reactions. Comparison of the prepared Fe-Al-Cu catalysts with bare Fe or Fe-Al ones indicated that reducibility was the most important factor influencing catalytic performance in the WGS reaction. Fe, Al, and Cu precursor concentrations of 0.126, 0.015, and 0.015 M, respectively, were used for large-scale synthesis, and the obtained catalyst (FAC-PC-3-240) exhibited BET surface area, reducibility, and Cu dispersion similar to those of FAC-PC-3, whereas the Fe₃O₄ crystallite size slightly increased upon scale-up. Comparative activity testing of FAC-PC-3-240 and commercial Fe-Cr at different GHSVs (3000 and 40,057 mL·g⁻¹·h⁻¹) revealed that the better catalytic performance of the former catalyst at high GHSV could be ascribed to the promotional effect of Cu on the easier reducibility of Fe species and the formation of additional Cu active sites. The performance of the FAC-PC-3-240 catalyst synthesized by controlling precursor concentration successfully proved the possibility of Cr substitution and demonstrated the excellent ability of this catalyst to promote the conversion of waste-derived synthesis gas into H₂.

Acknowledgements

This work was supported by the National Research Foundation of Korea grant funded by the Korea government (MSIP) (2017R1A2B4A007145). This

research was supported by Basic Science Research Program through the National Research Foundation of Korea (NRF) funded by the Ministry of Science, ICT & Future Planning (2019R1C1C1005022).

Appendix A. Supplementary data

Supplementary material related to this article can be found, in the online version, at doi:<https://doi.org/10.1016/j.apcatb.2019.02.036>.

References

- [1] S. Senkan, Combinatorial heterogeneous catalysis - a new path in an old field, *Angew. Chem. - Int. Ed.* 40 (2001) 312–329.
- [2] N. García-Moncada, M. González-Castaño, S. Ivanova, M. Ángel Centeno, F. Romero-Sarria, J. Antonio Odriozola, New concept for old reaction: novel WGS catalyst design, *Appl. Catal. B: Environ.* 238 (2018) 1–5.
- [3] D. Yao, Y. Zhang, P.T. Williams, H. Yang, H. Chen, Co-production of hydrogen and carbon nanotubes from real-world waste plastics: influence of catalyst composition and operational parameters, *Appl. Catal. B: Environ.* 221 (2018) 584–597.
- [4] M. Swati, T. Rema, K. Joseph, Hazardous organic compounds in urban municipal solid waste from a developing country, *J. Hazard. Mater.* 160 (2008) 213–219.
- [5] OECD, OECD Environmental Performance Reviews: Korea 2017, OECD Publishing, Paris, 2017.
- [6] W.-S. Yang, J.-K. Park, S.-W. Park, Y.-C. Seo, Past, present and future of waste management in Korea, *J. Mater. Cycles Waste Manag.* 17 (2015) 207–219.
- [7] Ministry of Environment Korea, Environmental Statistics Yearbook 2016, Ministry of Environment Korea, Sejong, 2017.
- [8] C.-Y. Lee, S.-Y. Huh, Forecasting new and renewable energy supply through a bottom-up approach: the case of South Korea, *Renew. Sustain. Energy Rev.* 69 (2017) 207–217.
- [9] O.A.Z. Sahraei, F. Larachi, N. Abatzoglou, M.C. Iliuta, Hydrogen production by glycerol steam reforming catalyzed by Ni-promoted Fe/Mg-bearing metallurgical wastes, *Appl. Catal. B: Environ.* 219 (2017) 183–193.
- [10] P.H. Wallman, C.B. Thorsness, J.D. Winter, Hydrogen production from wastes, *Energy* 23 (1998) 271–278.
- [11] D.-W. Jeong, V. Subramanian, J.-O. Shim, W.-J. Jang, Y.-C. Seo, H.-S. Roh, J.H. Gu, Y.T. Lim, High-temperature water gas shift reaction over Fe/Al/Cu oxide based catalysts using simulated waste-derived synthesis gas, *Catal. Lett.* 143 (2013) 438–444.
- [12] D.-W. Jeong, W.-J. Jang, J.-O. Shim, W.-B. Han, K.-W. Jeon, Y.-C. Seo, H.-S. Roh, J.H. Gu, Y.T. Lim, A comparison study on high-temperature water-gas shift reaction over Fe/Al/Cu and Fe/Al/Ni catalysts using simulated waste-derived synthesis gas, *J. Mater. Cycles Waste Manag.* 16 (2014) 650–656.
- [13] W.-J. Jang, H.-M. Kim, J.-O. Shim, S.-Y. Yoo, K.-W. Jeon, H.-S. Na, Y.-L. Lee, D.-W. Jeong, J.W. Bae, I.W. Nah, H.-S. Roh, Key properties of Ni-MgO-CeO₂, Ni-MgO-ZrO₂ and Ni-MgO-Ce_{(1-x)Zr_xO₂ catalysts for the reforming of methane with carbon dioxide, *Green Chem.* 20 (2018) 1621–1633.}
- [14] W.-J. Jang, D.-W. Jeong, J.-O. Shim, H.-M. Kim, H.-S. Roh, I.H. Son, S.J. Lee, Combined steam and carbon dioxide reforming of methane and side reactions: thermodynamic equilibrium analysis and experimental application, *Appl. Energy* 173 (2016) 80–91.
- [15] S. Navarro-Jaén, F. Romero-Sarria, M.A. Centeno, O.H. Laguna, J.A. Odriozola, Phosphate-type supports for the design of WGS catalysts, *Appl. Catal. B: Environ.* 244 (2019) 853–862.
- [16] Q. Zhang, L. Pastor-Pérez, W. Jin, S. Gu, T.R. Reina, Understanding the promoter effect of Cu and Cs over highly effective β-Mo₂C catalysts for the reverse water-gas shift reaction, *Appl. Catal. B: Environ.* 244 (2019) 889–898.
- [17] L. Pastor-Pérez, V. Belda-Alcázar, C. Marinib, M.M. Pastor-Blasa, A. Sepúlveda-Escribano, E.V. Ramos-Fernandez, Effect of cold Ar plasma treatment on the catalytic performance of Pt/CeO₂ in water-gas shift reaction (WGS), *Appl. Catal. B: Environ.* 225 (2018) 121–127.
- [18] H. Yan, X.-T. Qin, Y. Yin, Y.-F. Teng, Z. Jin, C.-J. Jia, Promoted Cu-Fe₃O₄ catalysts for low-temperature water gas shift reaction: optimization of Cu content, *Appl. Catal. B: Environ.* 226 (2018) 182–193.
- [19] C. Ratnasamy, J.P. Wagner, Water gas shift catalysis, *Catal. Rev. - Sci. Eng.* 51 (2009) 325–440.
- [20] C. Bosch, W. Wild, Producing hydrogen, US Patent US1115776A (1914).
- [21] F. Meshkani, M. Rezaei, Preparation of mesoporous nanocrystalline iron based catalysts for high temperature water gas shift reaction: effect of preparation factors, *Chem. Eng. J.* 260 (2015) 107–116.
- [22] M. Zhu, T.C.R. Rocha, T. Lunkenbein, A. Knop-Gericke, R. Schlögl, I.E. Wachs, Promotion mechanisms of iron oxide-based high temperature water-gas shift catalysts by chromium and copper, *ACS Catal.* 6 (2016) 4455–4464.
- [23] M. Zhu, I.E. Wachs, Iron-based catalysts for the high-temperature water-gas shift (HT-WGS) reaction: a review, *ACS Catal.* 6 (2016) 722–732.
- [24] C.J. Ketrakis, M. Zhu, E.K. Gibson, M. Daturi, F. Tao, A.I. Frenkel, I.E. Wachs, Dynamics of CrO₃-Fe₂O₃ catalysts during the high-temperature water-gas shift reaction: molecular structures and reactivity, *ACS Catal.* 6 (2016) 4786–4798.
- [25] M. Zhu, Ö. Yalçın, I.E. Wachs, Revealing structure-activity relationships in chromium free high temperature shift catalysts promoted by earth abundant elements, *Appl. Catal. B: Environ.* 232 (2018) 205–212.
- [26] P.C. Grevatt, Toxicological Review of Hexavalent Chromium, Report No. 18540-29-

- 9, U.S. Environmental Protection Agency (EPA), Washington, D.C., 1998.
- [27] Occupational Safety and Health Administration (OSHA), Hexavalent chromium, Report No. 3373-10, U.S. Department of Labor, 2009.
- [28] G.C. Chinchin, Catalytic preparation of hydrogen from carbon monoxide and water, EP Patent EP0062410B1 (1986).
- [29] H. Yan, X.-T. Qin, Y. Yin, Y.-F. Teng, Z. Jin, C.-J. Jia, Promoted Cu-Fe₃O₄ catalysts for low-temperature water gas shift reaction: optimization of Cu content, Appl. Catal. B: Environ. 226 (2018) 182–193.
- [30] V.D.B.C. Dasireddy, B. Likozar, J. Valand, Preferential oxidation of CO in H₂/H₂O/CO₂ water-gas shift feedstocks over Cu-based carbon nanotubes-supported heterogeneous catalysts, Appl. Catal. B: Environ. 239 (2018) 1044–1058.
- [31] G.C. De Araújo, M. Do Carmo Rangel, Environmental friendly dopant for the high-temperature shift catalysts, Catal. Today 62 (2000) 201–207.
- [32] S. Natesakhawat, X. Wang, L. Zhang, U.S. Ozkan, Development of chromium-free iron-based catalysts for high-temperature water-gas shift reaction, J. Mol. Catal. A Chem. 260 (2006) 82–94.
- [33] L. Zhang, X. Wang, J.M.M. Millet, P.H. Matter, U.S. Ozkan, Investigation of highly active Fe-Al-Cu catalysts for water-gas shift reaction, Appl. Catal. A Gen. 351 (2008) 1–8.
- [34] L. Zhang, J.M.M. Millet, U.S. Ozkan, Effect of Cu loading on the catalytic performance of Fe-Al-Cu for water-gas shift reaction, Appl. Catal. A Gen. 357 (2009) 66–72.
- [35] Z. Bao, W. Ding, Q. Li, Effect of Fe/Cu ratio on the activity of Fe-Al-Cu catalysts for water gas shift reaction under hydrogen-rich atmosphere, Int. J. Hydrogen Energy 37 (2012) 951–955.
- [36] Y. Ye, L. Wang, S. Zhang, Y. Zhu, J. Shan, F. Tao, The role of copper in catalytic performance of a Fe-Cu-Al-O catalyst for water gas shift reaction, Chem. Commun. (Camb.) 49 (2013) 4385–4387.
- [37] Z. Fu, J. Wang, N. Zhang, Y. An, Z. Yang, Effect of Cu doping on the catalytic activity of Fe₃O₄ in water-gas shift reactions, Int. J. Hydrogen Energy 40 (2015) 2193–2198.
- [38] M. Estrella, L. Barrio, G. Zhou, X. Wang, Q. Wang, W. Wen, J.C. Hanson, A.I. Frenkel, J.A. Rodriguez, In situ characterization of CuFe₂O₄ and Cu/Fe₃O₄ water-gas shift catalysts, J. Phys. Chem. C 113 (2009) 14411–14417.
- [39] X. Lin, R. Li, Y. Zhang, Y. Zhan, C. Chen, Q. Zheng, J. Ma, The role of surface copper species in Cu-Fe composite oxide catalysts for the water gas shift reaction, Int. J. Hydrogen Energy 40 (2015) 1735–1741.
- [40] D.-W. Jeong, A. Jha, W.-J. Jang, W.-B. Han, H.-S. Roh, Performance of spinel ferrite catalysts integrated with mesoporous Al₂O₃ in the high temperature water-gas shift reaction, Chem. Eng. J. 265 (2015) 100–109.
- [41] H.-S. Na, D.-W. Jeong, W.-J. Jang, J.-O. Shim, H.-S. Roh, The effect of preparation method on Fe/Al/Cu oxide-based catalyst performance for high temperature water gas shift reaction using simulated waste-derived synthesis gas, Int. J. Hydrogen Energy 40 (2015) 12268–12274.
- [42] S. Mitchell, N.-L. Michels, J. Pérez-Ramírez, From powder to technical body: the undervalued science of catalyst scale up, Chem. Soc. Rev. 42 (2013) 6094–6112.
- [43] H. Okudera, A. Yoshiasa, K. Murai, M. Okube, T. Takeda, S. Kikkawa, Local structure of magnetite and maghemite and chemical shift in Fe K-edge XANES, J. Miner. Petrol. Sci. 107 (2012) 127–132.
- [44] G. Vlaic, R. Di Monte, P. Fornasiero, E. Fonda, J. Kašpar, M. Graziani, Redox property-local structure relationships in the Rh-loaded CeO₂-ZrO₂ mixed oxides, J. Catal. 182 (1999) 378–389.
- [45] A. Grosman, C. Ortega, Capillary condensation in porous materials. Hysteresis and interaction mechanism without pore blocking/percolation process, Langmuir 24 (2008) 3977–3986.
- [46] M.R. Anantharaman, K. Seshan, S.N. Shringi, H.V. Keer, Development of pure and doped gamma ferric oxide, Bull. Mater. Sci. 6 (1984) 59–64.
- [47] D. Varisli, C. Korkusuz, T. Dogu, Microwave-assisted ammonia decomposition reaction over iron incorporated mesoporous carbon catalysts, Appl. Catal. B: Environ. 201 (2017) 370–380.
- [48] A.P. Grosvenor, B.A. Kobe, M.C. Biesinger, N.S. McIntyre, Investigation of multiplet splitting of Fe 2p XPS spectra and bonding in iron compounds, Surf. Interface Anal. 36 (2004) 1564–1574.
- [49] F. Heinrich, C. Schmidt, E. Löffler, M. Menzel, W. Grünert, Fe-ZSM-5 catalysts for the selective reduction of NO by isobutane - the problem of the active sites, J. Catal. 212 (2002) 157–172.
- [50] J.Y.C. Chen, J.T. Miller, J.B. Gerken, S.S. Stahl, Inverse spinel NiFeAlO₄ as a highly active oxygen evolution electrocatalyst: promotion of activity by a redox-inert metal ion, Energy Environ. Sci. 7 (2014) 1382–1386.
- [51] E. Pellegrini, M. Hagelstein, S. Doyle, H.O. Moser, J. Fuchs, D. Vollath, S. Schuppler, M.A. James, S.S. Saxena, L. Niesen, O. Rogojanu, G.A. Sawatzky, C. Ferrero, M. Borowski, O. Tjernberg, N.B. Brookes, Characterization of nanocrystalline γ-Fe₂O₃ with synchrotron radiation techniques, Phys. Status Solidi B 215 (1999) 797–801.
- [52] M. Wilke, F. Farges, P.E. Petit, G.E. Brown, F. Martin, Oxidation state and coordination of Fe in minerals: an Fe K-XANES spectroscopic study, Am. Miner. 86 (2001) 714–730.
- [53] G.S. Henderson, F.M.F. De Groot, B.J.A. Moulton, X-ray absorption near-edge structure (XANES) spectroscopy, Rev. Miner. Geochem. 78 (2014) 75–138.
- [54] A. Kuzmin, J. Chaboy, EXAFS and XANES analysis of oxides at the nanoscale, IUCrJ 1 (2014) 571–589.
- [55] C. Piquier, M.A. Laguna-Marco, A.G. Roca, R. Boada, C. Guglieri, J. Chaboy, Fe K-edge X-ray absorption spectroscopy study of nanosized nominal magnetite, J. Phys. Chem. C 118 (2014) 1332–1346.
- [56] F. Jiao, J.-C. Jumas, M. Womes, A.V. Chadwick, A. Harrison, P.G. Bruce, Synthesis of ordered mesoporous Fe₃O₄ and γ-Fe₂O₃ with crystalline walls using post-tem-plate reduction/oxidation, J. Am. Chem. Soc. 128 (2006) 12905–12909.
- [57] L.R. Winter, E. Gomez, B. Yan, S. Yao, J.G. Chen, Tuning Ni-catalyzed CO₂ hydrogenation selectivity via Ni-ceria support interactions and Ni-Fe bimetallic formation, Appl. Catal. B: Environ. 224 (2018) 442–450.
- [58] J. Yang, J. Wang, W. Pan, T. Regier, Y. Hu, C. Rumpel, N. Bolan, D. Sparks, Retention mechanisms of citric acid in ternary kaolinite-Fe(III)-citrate acid systems using Fe K-edge EXAFS and L_{3,2}-edge XANES spectroscopy, Sci. Rep. 6 (2016) 1–9.
- [59] F. Caddeo, D. Loche, M.F. Casula, A. Corrias, Evidence of a cubic iron sub-lattice in t-CuFe₂O₄ demonstrated by X-ray absorption fine structure, Sci. Rep. 8 (2018) 797–809.
- [60] H. Okudera, K. Kihara, T. Matsumoto, Temperature dependence of structure parameters in natural magnetite: single-crystal X-ray studies from 126 to 773K, Acta Crystallogr. B52 (1996) 450–457.
- [61] F. Jiao, H. Yen, G.S. Hutchings, B. Yonemoto, Q. Lu, F. Kleitz, Synthesis, structural characterization, and electrochemical performance of nanocast mesoporous Cu-/Fe-based oxides, J. Mater. Chem. A 2 (2014) 3065–3071.
- [62] A. Khan, P. Chen, P. Boolchand, P.G. Smirniotis, Modified nano-crystalline ferrites for high-temperature WGS membrane reactor applications, J. Catal. 253 (2008) 91–104.
- [63] G.K. Reddy, K. Gunasekera, P. Boolchand, J. Dong, P.G. Smirniotis, High temperature water gas shift reaction over nanocrystalline copper codoped-modified ferrites, J. Phys. Chem. C 115 (2011) 7586–7595.
- [64] G.K. Reddy, P. Boolchand, P.G. Smirniotis, Unexpected behavior of copper in modified ferrites during high temperature WGS reaction-Aspects of Fe³⁺ ↔ Fe²⁺ redox chemistry from Mössbauer and XPS studies, J. Phys. Chem. C 116 (2012) 11019–11031.
- [65] W.-J. Jang, H.-S. Roh, D.-W. Jeong, An important factor for the water gas shift reaction activity of Cu-loaded cubic Ce_{0.8}Zr_{0.2}O₂ catalysts, Environ. Eng. Res. 23 (2018) 339–344.
- [66] V.D.B.C. Dasireddy, B. Likozar, J. Valand, Preferential oxidation of CO in H₂/H₂O/CO₂ water-gas shift feedstocks over Cu-based carbon nanotubes-supported heterogeneous catalysts, Appl. Catal. B: Environ. 237 (2018) 1044–1058.